

Placental vascular alterations lead to early neurodevelopmental and pulmonary impairment in the rabbit fetal growth restriction model

Ignacio Valenzuela

KU Leuven

David Basurto

KU Leuven

Yannick Regin

KU Leuven

Andre Gie

Stellenbosch University and Tygerberg Hospital

Lennart van der Veeke

KU Leuven

Simen Vergote

KU Leuven

Emma Muñoz-Moreno

Institut d'Investigacions Biomèdiques August Pi i Sunyer (IDIBAPS)

Bartosz Leszczynski

Jagiellonian University

Jan Deprest (✉ jan.deprest@uzleuven.be)

KU Leuven

Johannes Merwe

KU Leuven

Article

Keywords:

Posted Date: April 15th, 2022

DOI: <https://doi.org/10.21203/rs.3.rs-1522660/v1>

License:   This work is licensed under a Creative Commons Attribution 4.0 International License.

[Read Full License](#)

Abstract

Fetal growth restriction is one of the leading causes of perinatal mortality and morbidity and has consequences that extend well beyond the neonatal period. Current management relies on timely delivery rather than improving placental function. Several prenatal strategies have failed to show benefit in clinical trials after promising results in animal models. Most of these animal models have important developmental and structural differences compared to the human and/or are insufficiently characterized. We aimed to describe placental function and structure in an FGR rabbit model, and to characterize the early brain and lung developmental morbidity using a multimodal approach. FGR was induced in time-mated rabbits at gestational day 25 by partial uteroplacental vessel ligation in one horn. Umbilical artery Doppler was measured before caesarean delivery at gestational day 30, and placentas were harvested for computed microtomography and histology. Neonates underwent neurobehavioral or pulmonary functional assessment the day after delivery, followed by brain or lung harvesting, respectively. Neuropathological assessment included multiregional quantification of neuron density, apoptosis, astrogliosis, cellular proliferation, and oligodendrocyte progenitors. Brain region volumes and diffusion metrics were obtained from ex-vivo brain magnetic resonance imaging. Lung assessment included biomechanical tests and pulmonary histology. Fetal growth restriction was associated with labyrinth alterations in the placenta, driven by fetal capillary reduction, and overall reduced vessels volume. FGR caused altered neurobehavior paralleled by regional neuropathological deficits and reduced fractional anisotropy in the cortex, white matter, and hippocampus. In addition, FGR kittens presented functional alterations in the peripheral lung and structurally underdeveloped alveoli. In conclusion, in a uteroplacental insufficiency FGR rabbit model, placental vascular alterations coincide with neurodevelopmental and pulmonary disruption.

Introduction

Fetal Growth Restriction (FGR) refers to the inability of a fetus to achieve its genetic growth potential¹. It is one of the main contributors to perinatal mortality and morbidity, and it is associated with almost 50% of stillbirth cases worldwide²⁻⁴. Beyond the neonatal period, it causes cognitive and behavioral impediment in childhood⁵ and metabolic, pulmonary, and cardiovascular disease in adult life^{6,7}. The main cause of FGR is uteroplacental insufficiency (UPI), a condition whereby a defective placental development leads to an insufficient supply of oxygen and nutrients to support the developing fetus, resulting in acidosis, hypoxemia, and in more severe cases ultimately intrauterine fetal demise. There is currently no effective prenatal treatment for FGR: clinical trials have failed to deliver a safe and effective therapy, even after successful preclinical studies⁸⁻¹⁰. Well characterized animal models with developmental, functional, and structural similarities to the human are fundamental to understand the consequences of FGR and to design new therapeutic strategies aimed at ameliorating them.

Several animal models have been described but so far no single animal model mimics the entire spectrum of human FGR¹¹. In recent years, the rabbit has been established as a well-rounded, versatile

model for perinatal conditions¹²⁻¹⁸. Like humans and rodents, they have discoid, haemochorial placentas, in which maternal blood is in direct contact with the trophoblast. Furthermore, only two trophoblast layers separate maternal and fetal blood spaces (hemo-dichorial placenta), closing the gap between the murine hemo-trichorial and the human hemo-monochorial placentas¹⁹. Trophoblast volumes, placental glucose transporters, and other pregnancy-specific changes in the rabbit have also been shown to mimic the clinical scenario²⁰.

In addition to the morphological and functional placental similarities, rabbits resemble humans closer than other species in terms of neurodevelopment. Neurogenesis starts in the first trimester, and white matter maturation begins around birth to continue through the first year of life^{21,22}. Pulmonary development is also a perinatal process, with alveolarization beginning prior to birth, so that at term rabbit lungs are in the terminal air sac stage²³⁻²⁵. In addition to that, rabbits have several practical benefits; they are non-seasonal in mating habits, have a short gestation period with a large litter size, and are suitable for foster care and follow-up assessment.

Our group has utilized and refined a robust neurodevelopmental and pulmonary multimodal evaluation platform to assess newborn and preadolescent rabbits and phenotype the effects of bronchopulmonary dysplasia²⁶⁻²⁹, prematurity^{30,31}, and congenital diaphragmatic hernia^{32,33}. Herein, we characterize the consequences of FGR induced by uteroplacental vessel ligation (UPVL) in placental microvasculature, and early brain and lung development in the rabbit model.

Results

UPVL induces FGR and alters labyrinth zone vascularization

Twenty-two does delivered 65 live kittens from the ligated horns, and 86 from the control horns. UPVL resulted in higher intrauterine mortality ($p < 0.0001$) and a significant reduction in body weight ($p < 0.0001$), placental weight ($p = 0.0002$), and fetal/placental weight ratio ($p < 0.0001$) (Table 1). Umbilical artery pulsatility index was not significantly different between groups (1.85 ± 0.4 vs. 1.77 ± 0.3 ; $p = 0.6$).

Table 1
Survival and biometrics

n = 22 does	FGR	Control	P-value
Survival	65/130 (50%)	86/97 (89%)	< 0.0001
Birth weight (g)	33.65 ± 5.97	44.14 ± 7.68	< 0.0001
Placental weight (g)	5.33 ± 0.85	6.08 ± 1.04	0.0002
Brain weight (g)	1.50 ± 0.25	1.80 ± 0.14	< 0.0001
Brain/body weight ratio	0.0456 ± 0.005	0.0407 ± 0.007	0.0007
Fetal/placental weight ratio	6.41 ± 1.07	7.30 ± 1.07	< 0.0001

Survival and birth weight were assessed 4 hours after caesarian delivery. Brain weight was measured at PND1. Data expressed as mean ± SD. FGR: fetal growth restriction.

At histological assessment placentas from FGR kittens had a significantly smaller labyrinth zone when compared to controls ($p < 0.0001$) (Fig. 1A). Within the FGR labyrinths, the proportion of fetal capillaries was significantly reduced ($p < 0.0001$), and the proportion of maternal blood spaces significantly increased ($p < 0.0001$) (Fig. 1A). Microvasculature assessment by computerized tomography showed FGR placentas had significantly reduced vessel volume after correction for placental weight ($p = 0.015$) (Fig. 1B). The vessel surface area and the distribution of vessels according to their diameter was not significantly different between groups.

Figure 1. Placental histology and microcomputed tomography. A. Placenta with cytokeratin/lectin double staining, divided by placental zones (left image). Within the labyrinth (zoomed), fetal capillaries (star), maternal blood spaces (arrow) and trophoblast (arrowhead) were grid counted and expressed as relative areas. B. Representative image of placental microcomputed tomography after color coding according to vessel diameter. Data displayed as mean ± SD with significance as * $0.05 \geq p > 0.01$; ** $0.01 \geq p > 0.001$.; *** $0.001 > p > 0.0001$; **** $p < 0.0001$.

FGR is associated with early neurodevelopmental impairment.

FGR led to a significant reduction in brain weight ($p < 0.0001$) and increased brain to body weight ratio ($p = 0.0007$) at birth (Table 1). FGR was also associated with motoric and sensory deficits on neurobehavioral assessment (NBA), as displayed in Fig. 2A. FGR kittens had abnormal posture, gait, and locomotion, but activity duration was similar to controls. Additionally, FGR led to hampered cranial nerves activity, pain response, and righting reflex.

FGR kittens have lower multiregional neuron density, associated with increased apoptosis and astrogliosis, and reduced oligodendrocyte precursor cells.

As in Fig. 2B, FGR led to a significant reduction in neuron density in the frontal cortex ($p = 0.00002$), corpus callosum ($p = 0.006$), caudate nucleus ($p = 0.005$), putamen ($p = 0.02$), cornu ammonis 1 (CA1; $p = 0.0008$), cornu ammonis 3 (CA3; $p = 0.00003$), dentate gyrus ($p = 0.00005$), and anteroventral thalamic nuclei ($p = 0.003$). This coincided with an increased proportion of TUNEL-positive cells in the corpus callosum ($p = 0.02$), CA1 ($p = 0.001$), CA3 ($p = 0.02$) and whole hippocampus ($p = 0.003$) in FGR brains (Fig. 2C). Additionally, rabbits from the FGR group had a higher proportion of GFAP-positive cells in the corpus callosum ($p = 0.0005$) and dentate gyrus ($p = 0.01$) (Fig. 2C). NG-2 positive cells were significantly decreased in the caudate nucleus ($p = 0.02$) and corpus callosum ($p = 0.04$) (Supplementary materials, Fig. S1). No significant differences were found in Ki67-positive cells in the same regions (Fig. S2).

Figure 2. Brain assessment in postnatal day 1 rabbits. A. Examples of neurobehavioral tests, and individual scores. B. Neuron density was assessed with cresyl violet stained slides in the depicted areas. C. Representative images of apoptosis (TUNEL), and astrogliosis (GFAP) in hippocampus and corpus callosum, respectively. FC: frontal cortex; CC: corpus callosum; CN: caudate nucleus; P: putamen; CA1: cornu ammonis 1; CA3: cornu ammonis 3; DG: dentate gyrus; AVTN; anteroventral thalamic nuclei. Data displayed as median and IQR (A) or mean and SD (B, C) with significance as $*0.05 \geq p > 0.01$; $** 0.01 \geq p > 0.001$; $***0.001 > p > 0.0001$; $**** p < 0.0001$.

Regional neuropathological changes coincide with MRI volumetric and diffusion weighted imaging.

T1-derived volumetric data from magnetic resonance imaging (MRI) showed that FGR rabbits had an overall lower absolute brain volume. However, after normalizing the regional volumes to their respective total brain volume, no differences were present between the two groups in the volume of specific brain regions.

Differences on diffusion tensor metrics also paralleled histological findings. Fractional anisotropy (FA) was globally reduced ($p = 0.03$), and additionally significantly lower in the frontal cortex ($p = 0.03$), corpus callosum ($p = 0.009$), internal capsule ($p = 0.02$), corona radiata ($p = 0.002$), hippocampus ($p = 0.02$), thalamus ($p = 0.02$) and hypothalamus ($p = 0.049$) in FGR rabbits, while there was no significant difference in the caudate nucleus and putamen (Fig. 3). Mean diffusivity (MD) was only found significantly reduced in the hippocampus ($p = 0.009$) (Fig. 3).

Figure 3. *Ex vivo* brain diffusion tensor metrics at postnatal day 1. Data displayed as median and IQR with significance as $*0.05 \geq p > 0.01$; $** 0.01 \geq p > 0.001$. Correction for multiple comparison by Benjamini, Krieger and Yekutieli method with 10% FDR.

FGR leads to significant alteration of peripheral lung mechanics and compliance

Lung function was significantly reduced in FGR animals. Forced oscillation tests showed increased tissue damping ($p < 0.0001$), tissue elastance ($p < 0.0001$), respiratory system resistance ($p < 0.0001$) and decreased dynamic compliance ($p < 0.01$) in FGR lungs, while central airway resistance was not

significantly different between groups (Fig. 4A). In pressure-volume perturbations, FGR lungs had significantly reduced hysteresis ($p = 0.002$) and static compliance ($p = 0.01$) compared to controls (Fig. 4B).

Figure 4. Pulmonary functional tests at postnatal day 1. A. Forced oscillation test results. B. Pressure/volume loop. C. Representative images of histological H&E-stained slides and alveolar architecture data. Data displayed as mean \pm SD, with significance as * $0.05 \geq p > 0.01$; ** $0.01 \geq p > 0.001$; *** $0.001 > p > 0.0001$; **** $p < 0.0001$.

FGR does not influence overall lung volume, but disrupts alveolar development

Both groups had similar lung sizes when corrected by body weight, as measured by water displacement (38.34 ± 7.17 vs. 39.08 ± 5.46 mL; $p = 0.7$) and inspiratory capacity (32.09 ± 5.80 vs. 34.08 ± 4.56 mL; $p = 0.2$). In contrast, on histological assessment FGR lungs had significantly decreased alveolar surface area (S; $p < 0.001$), increased alveolar size (Lm; $p = 0.02$), and increased alveolar airspace (Lma; $p < 0.02$), while septal thickness (Lmw) was similar between groups (Fig. 4C). The medial thickness of the peripheral pulmonary arteries was also comparable between groups (Supplementary materials, Fig. S3).

All the exact values from histological assessment (placenta, brain and lungs), brain MRI, and PFA, are added to Supplementary materials.

Discussion

This study expands the characterization of the rabbit FGR model as previously described^{12,16} by utilizing a multimodal assessment approach, adding a description of placental microvascular changes, and subsequent early functional and structural alterations in the brain and lungs. In this model the exchange zone area -the labyrinth- and overall vessel volume in FGR placentas are significantly reduced. Upon neuropathological review, lower neuron density and higher apoptosis coincide with reduced fractional anisotropy in grey and white matter structures and are associated with neurobehavioral deficits. Furthermore, lung parenchymal functional and structural changes are demonstrated for the first time in this FGR model. Herein the reduction in alveolar surface area accompanies the increased resistance and damping in the peripheral lungs.

Underdevelopment of the labyrinth is the most notable finding in the placenta. This was driven by a reduction in fetal capillaries at histological level and coincided with the reduction in fetoplacental vessel volume on microcomputed tomography. Although this is the first published experience using this technique in the rabbit, labyrinth alterations have been previously described in several other FGR models, including those induced by maternal undernutrition³⁴, exogenous^{35,36} and endogenous³⁷ glucocorticoid excess, heavy metal exposure³⁸, NO synthetase inhibition³⁹, and systemic inflammation⁴⁰. Furthermore, labyrinth underdevelopment, and particularly fetal vessel reduction, has been associated with reduced levels of different placental vascular endothelial growth factor (*VEGF*) mRNAs³⁶, and glucose transport

capacity^{37,41}. Future placental characterization in this model to include the expression of these and other key genes might help unravel the complex molecular machinery behind placental development and function in uteroplacental insufficiency.

The pulmonary morbidity in this study is likely the result of uteroplacental insufficiency and not directly caused by toxins or drugs, as in other models^{42,43}. Moreover, the pulmonary impairment was not influenced by prematurity or postnatal lung injury, commonly present in perinatal lung assessment. The rabbit mimics human pulmonary developmental closer than other species as alveolarization is a perinatal process⁴⁴, and not entirely prenatal as in sheep and guinea pigs, or postnatal as in rats and mice. Nonetheless, our results are consistent with findings in murine and ovine models⁴⁵⁻⁴⁸, and suggest FGR disrupts alveolar development and leads to biomechanical dysfunction, but does not affect lung volume. The functional impairment was observed in both forced oscillation and pressure-volume maneuvers. On the former, increased tissue damping, tissue elastance and respiratory system resistance indicate peripheral remodeling. The similar central airway resistance suggests comparable large airways caliber and is in line with the timing of the placental insult after the formation of the central airways. The decreased hysteresis and poorer compliance found on pressure-volume maneuvers indicate that FGR results in stiffer lungs and that the work of breathing is higher in this group. Structural data is in line with the biomechanical findings and coincides in a peripheral lung alteration, showing a simplified alveolar morphology, with increased airspace size and lower alveolar surface area available for gas exchange.

The molecular and cellular drivers underlying these changes are likely multiple and complex, and their description was not the purpose on this model characterization. They will, however, need to be approached and compared against findings in other models, which include dysregulation of *VEGF*^{45,47}, retinoic acid receptors^{49,50}, and other pathways involved in hypoxia signaling^{51,52}, tissue repair, and cellular communication regulation⁵³. Additionally, it will be of interest to determine if these functional and structural alterations are sustained in the longer term, or if any new pulmonary findings develop overtime.

Regarding neurodevelopmental assessment, the neurobehavioral deficit we describe is in line with previous reports in the rabbit^{54,55} and other animal models⁵⁶⁻⁵⁸, highlighting the cross-species nature of these findings. Furthermore, the neurobehavioral deficit correlated with lower neuron density at neuropathology and altered structural integrity at MRI. Interestingly, these findings were significant in the cortex, white matter regions, and hippocampus, yet the caudate nucleus and putamen seem to be less affected. This coincides with regional variations in brain perfusion described in the context of brain sparing in severe FGR⁵⁹ with preferential supply of blood flow to the deep grey matter of the basal ganglia in detriment of the frontal lobe. Reduced fractional anisotropy, lower neuron density, and increased apoptosis in these regions suggest structural integrity is compromised in FGR brains even before myelination takes place⁶⁰. Organization in neuronal population, followed by axonal and dendritic growth, increase density in these areas, thus an insult to neuronal organization might reduce FA independent of myelination.

We acknowledge our study has limitations. First, the acute induction of UPI does not mimic the slow progressive nature of FGR. However, most models with an earlier and/or more persistent induction, like maternal undernutrition or glucocorticoid excess, either fail to recreate the severity of FGR, or expose the fetus to insults not related to placental function. Similarly, attempts to reproduce the progressiveness of UPI in surgical models have failed to mimic the severity on the disease by increased fetal mortality^{61,62}. Secondly, this model describes the effects of FGR in near-term neonates, even though most severe clinical cases require preterm delivery. Pulmonary and neurodevelopment are highly dependent on GA at delivery, and thus assessing near-term neonates allows us to unmask the effects of FGR from those of prematurity. Lastly, only immediate neonatal consequences of FGR are reported in the current study. We are aware that our findings need to be supplemented with observations on the mid and long-term, and that further assessment is a necessary next step into the robust characterization of the rabbit model, and we are currently working towards such characterization.

In conclusion, in the rabbit UPVL FGR model we demonstrated that placental vascular alterations lead not only to neurodevelopmental but also pulmonary deficits in the early neonatal period. A longitudinal FGR model characterization of placental, neurocognitive, and pulmonary function and structure could greatly aid in assessing the safety and efficacy of novel therapeutic strategies.

Materials And Methods

Animal model

All animals were treated according to current guidelines for animal well-being, and experiments were approved by the Ethics Committee for Animal Experimentation of the Faculty of Medicine (P080/2019). Experiments are reported according to ARRIVE guidelines⁶³. Time-mated rabbits (hybrid of Dendermonde and New Zealand White) were housed in individual cages at 21°C, 42% humidity, with a 12-hour day/night cycle and free access to food and water. Conception day was considered day 0 of pregnancy (GA = 0). At GA 25 (full term 31.5 days), does underwent induction of FGR. Briefly, rabbits were administered induction anesthesia with IM ketamine (35 mg/kg Nimatek®, Eurovet Animal Health BV, Bladel, The Netherlands) and xylazine (5 mg/kg XYL-M® 2%, VMD, Arendonk, Belgium), and antibiotic prophylaxis (10 mg/kg Baytril® 2.5% SC, Bayer, Diegem, Belgium), tocolysis (10 mg/kg Depo-Provera® SC, Pfizer, Puurs, Belgium), and analgesia (0.03 mg/kg Vetergesic® SC, Ceva Animal Health, Brussels, Belgium) prior to surgery. Anesthesia was maintained with a continuous IV infusion of ketamine (8-16mg/kg/h) and xylazine (2.4-4.8mg/kg/h), while monitoring vital signs. Following laparotomy, 30–40% of the vessels going to each placenta were ligated in one random horn with Vicryl® 5 – 0 (Ethicon®, Diegem, Belgium), leaving the contralateral unligated horn as internal control. The abdomen was closed with Vicryl® 2 – 0 and Monocryl® 3 – 0 (Ethicon®, Diegem, Belgium) for fascia and skin, respectively. The surgical wound was infiltrated with levobupivacaine (2 mg/kg Chirocaine®, Abbvie, Wavre, Belgium) and sprayed with aluminium (Kela®, Hoogstraten, Belgium).

Rabbits were monitored daily until delivery by caesarian section at GA 30. Following delivery, does were euthanized using IV phenytoin/pentobarbital (140 mg/kg Euthasol®, Kela, Bladel, The Netherlands). Kittens were pet dried, numbered with a permanent marker, and kept in a warmed (34°C) and humidified (55% RH) incubator. Later that day they were stimulated to urinate, weighed, and fed a commercial milk substitute (Day One, protein 30%, fat 50%; Fox Valley, Lakemoor, IL) with added probiotics (Bio-Lapis; Probiotics International, Somerset, UK) and immunoglobulins (Col-o-Cat; SanoBest, Hertogenbosch, The Netherlands). The following morning litters were allocated for brain or lung assessment.

Placental ultrasound

At the time of caesarean delivery rabbits were anesthetized with the same protocol as for FGR induction, put on a warming pad under a warming light, and uterine horns were exposed and continuously rinsed with warm saline (37°C). The VisualSonics VEVO 2100 (Toronto, Ontario, Canada) high-resolution micro ultrasound platform and a VisualSonics MS-250 transducer were used for image acquisition (center frequency 21 MHz; bandwidth 13–24 MHz; geometric focus 15 mm; maximum image width 23 mm; maximum image depth 30 mm; footprint 28 x 5.75 mm). Flow velocity waveforms of the umbilical artery were obtained in both ovarian end fetuses by locating the umbilical vessels using color Doppler and placing the pulsed Doppler sample gate over the umbilical artery, keeping the angle to a minimum. The pulsatility index (PI) was calculated offline using the VisualSonics analysis software.

Placental histology

After delivery, placentas (until and including the decidua) were carefully separated from the implantation sites in the uterine wall, washed in PBS, trimmed from umbilical cord and membranes, and immerse-fixed in 4% paraformaldehyde (PFA) for 72h, blotted dry and weighed. The smallest lobe was sectioned in 2 coronal portions, embedded in paraffin blocks, and cut in 4µm slides. 2 slides per placenta were then double stained for cytokeratin and lectin to assess trophoblast and fetal capillaries. The detailed staining protocol is added in the Supplementary materials.

All slides were digitally scanned with the Zeiss AxioScan Z1 imaging platform (AxioScan® Slide Scanner, Carl Zeiss MicroImaging GmbH, Munich, Germany).

Placental zones (labyrinth, junction, decidua) were manually delineated using QuPath software⁶⁴ and their area relative to the total placental area was calculated. The structures within the labyrinth zone were manually quantified as described before⁶⁵. Briefly, using a 4x4 point counting grid on 16 random fields at 20x magnification, the number of maternal blood spaces, fetal capillaries, and trophoblast cells was quantified and expressed as a percentage of the total count. A blinded observer (I.V.) performed all histological evaluations.

Placental computed microtomography

A subset of rabbits was used for fetoplacental perfusion with a contrast agent under the same anesthesia protocol at GA30. Following laparotomy, both uterine horns were removed and immediately placed on ice. Fetuses and placentas were exposed, and a 24G cannula was inserted in the umbilical vein

of each fetus, while an umbilical artery was cut open to serve as vent. Initially, warm heparinized saline was perfused, followed by a barium-based contrast solution consisting of 0.9% sodium chloride solution, barium sulfate (E-Z PAQUE® High Density Barium Sulfate 98.75%, Bracco imaging, Milan, Italy), and porcine skin gelatin (Gelatin 48723, Sigma-Aldrich, Darmstadt, Germany), previously filtered and warmed to 60°C. Perfusion was stopped when the contrast solution was clearly seen in the capillary bed of the placenta. Thereafter, placentas were separated from the conceptuses and immersed in 4% PFA for 24h, washed, and stored in PBS. A total of 16 placentas (eight FGR and eight controls) from four different litters were included for analysis.

X-ray computed microtomography scans were performed using SkyScan 1172 micro-CT system (Bruker microCT, Kontich, Belgium) with X-ray energy of 80 keV. The image pixel size was set to 8.98 µm and a 0.5 mm Al filter was applied. Projection images were captured between the rotation steps of 0.2°. Each projection was merged from 6 or 8 images averaged from 5 frames to minimize the image noise and captured with different field of view to cover the entire sample, resulting in 3872 by 3872–4956 pixels. The total scan duration was up to 15h.

For image reconstruction, GPU powered NRecon software (v.1.7.3.2, Bruker micro-CT) was used. Image processing and analysis was done by CT analyzer software (v.1.20.3.0, Bruker micro-CT). The reconstructed image stacks were median filtered with 2 pixels circular kernel, and histogram based manual global threshold was applied. The distribution of vessels thickness, and parameters of volume and surface of vascular tree were calculated. Additionally, color-coding visualization of the local thickness was applied. An observer blinded to group assignment (B.L.) performed all evaluations.

Neurobehavioral assessment

On postnatal day 1 (PND1), kittens underwent a validated NBA protocol^{18,66}. Short-term motor assessment comprised scoring of gait, posture, locomotion, head and limb activity, and activity duration. Afterwards, the cranial nerves, pain response, and righting reflex were tested for sensory evaluation. All assessments were filmed and later scored by an observer blinded to the groups (I.V.). A full description of NBA protocols can be found in the Supplementary materials.

Brain harvesting

Immediately after NBA, animals were deeply sedated with IM ketamine (35 mg/kg) and xylazine (6 mg/kg), and transcardially perfused with 0.9% saline + heparin (100 u/mL; 3 minutes at 30mL/min) followed by 4% PFA (5 minutes at 30ml/min). Their brains were removed from the skull and further immerse fixed in 4% PFA for 48h. A subgroup of kittens (n = 23) was perfused with heparinized saline, followed by 4% PFA and 2% (10 mM) gadoteridol (ProHance® 1mL of 279,3mg/mL solution). Their brains were kept inside their craniums for a maximum of 7 days to undergo MRI, after which they were removed and processed for histological assessment.

Brain MRI

Ex vivo MRI was performed on perfused fixed brains using the active staining technique. Briefly, a Bruker Biospec 9.4 Tesla small animal MR scanner (Bruker Biospin, Ettlingen, Germany; horizontal bore, 20 cm) equipped with actively shielded gradients (600 mT/m) was used. Data was acquired using a 72mm internal diameter quadrature volume coil for transmission decoupled with a rat brain quadrature shaped surface coil for signal reception (volume resonator, Rapid Biomedical, Rimpfing, Germany). Data was acquired with a high-resolution 3D Flash sequence (TE/TR 5.5/50 ms; flip angle 70 degrees; slice thickness 0.35 mm with no interslice gap, data matrix 392×392×392; isotropic resolution 89µm; 4 averages, acquisition time 1h15min) and a SE-EPI sequence (8 segments; TE/TR: 25/150ms; slice thickness 0.4mm with no interslice gap, data matrix 192×160×160; isotropic spatial resolution of 208 µm; 64 directions and 3 b-values per direction of 800, 1000, 1500 s/mm², acquisition time 1h43min).

MRI volumes were processed to quantify microstructural properties in the following brain regions: frontal cortex, corpus callosum, caudate nucleus, putamen, internal capsule, corona radiata, hippocampus, thalamus, and hypothalamus. Automatic atlas-based parcellation was obtained by diffeomorphic registration of the atlas template in Ferraris et al ⁶⁷ to the acquired structural images, and then translated to the diffusion space. Fractional anisotropy (FA) and mean diffusivity (MD) were estimated using dipy python libraries^{68,69}, and their mean values in regions of interest were computed. An observer blinded to group assignment (E.M.) performed all evaluations. A complete description of MRI processing can be found in Supplementary materials.

Of 23 acquisitions (13 controls 10 FGR), 4 (2 in each group) were excluded from analysis due to important artifacts. Statistical comparison between groups was performed in one random cerebral hemisphere. An interim power calculation, based on the FA data in the hippocampus, confirmed a power of 95% to detect these differences.

Brain histology

Following fixation, brains were paraffin embedded and serially sectioned at 4 µm. Three sets of four serial coronal sections every 100 µm were taken at each of the following two levels, as previously described¹⁸: level 1 started at the medial septal nucleus and level 2 at the hippocampal formation.

Six slides per brain (three slides per level) were stained with Cresyl Violet (CV; C5042-10G; Sigma- Aldrich, Overijse, Belgium), and two slides per brain (one slide per level, eight slides in total) were incubated with each of the following four primary antibodies: mouse monoclonal anti-human Ki67 (M724001-2; Agilent, Diegem, Belgium), mouse monoclonal anti-glial fibrillary acidic protein antibody (GFAP) (G6171, Sigma-Aldrich, St Louis, MO, USA), anti-NG2 chondroitin sulfate proteoglycan antibody (MAB5384, Millipore, Billerica, MA, USA), or a terminal deoxynucleotidyl transferase dUTP nick end labeling (TUNEL) method for fluorescent in situ end labeling of double- stranded DNA fragmentation (Apoptag S7110; Millipore). The secondary antibody was Alexa Fluor® 488 goat anti-mouse conjugate (Invitrogen) or Alexa Fluor® 647 goat anti-mouse conjugate. Sections were counterstained with Hoechst 33342 (Sigma-Aldrich, Bornem, Belgium). Eight brain areas were assessed, namely, the frontal cortex, corpus callosum, caudate nucleus, putamen, hippocampus (CA1, CA3, dentate gyrus), and thalamus (anteroventral nucleus).

Details on image acquisition and quantification can be found in Supplementary materials.

Pulmonary function testing

Pressure-volume and forced oscillation maneuvers were performed via a tracheostomy on PND1 using the FlexiVent system (SciReq; FlexiVent, Montreal, QC, Canada). Animals were sedated with ketamine (35 mg/kg) and xylazine (6 mg/kg) before tracheostomy. An 18-gauge metal cannula was inserted into the trachea and secured with an airtight suture. Kittens were ventilated with a tidal volume of 10 mL/kg and positive end-expiratory pressure of 3 cmH₂O at a rate of 120 breaths/min. Before lung function tests, two deep inflation maneuvers were performed until reaching a pressure of 30 cmH₂O to maximally inflate the lungs and standardize lung volume. Both pressure-volume (inspiratory capacity, static compliance, and static elastance) and forced oscillation tests (tissue damping, tissue elastance, central airway resistance, respiratory system resistance, dynamic compliance, and dynamic elastance) were performed as previously described⁷⁰. The mean of three separate measurements for each maneuver, with a coefficient of determination > 95%, was calculated and used as a single data point for analysis.

Histological lung assessment.

After PFT, lungs were removed *en bloc* via thoracotomy, the trachea was cannulated with a 20-gauge catheter, and the left lung was pressure fixed for 24h at a constant hydrostatic pressure of 25 cmH₂O in 4% PFA⁷⁰. After fixation, left lung volume was calculated using water displacement before paraffin embedding. Alveolar morphology was measured on digitally scanned 5µm hematoxylin and eosin (H&E)-stained slides using a semi-automated, validated Fiji-plugin (ImageJ) (<http://fiji.sc/Fiji>) that randomly selected 20 fields per lung⁷¹, according to stereological principles. Calculations of mean linear intercept (Lm), alveolar air space (Lma), and interalveolar septal thickness (Lmw) were made as previously described²⁹. Vascular morphology was evaluated using immunohistochemistry. A primary α-smooth muscle actin (α-SMA) antibody (mouse anti-human, M0851; DakoCytomation, Glostrup, Denmark) was used in combination with a horseradish peroxidase-conjugated secondary antibody (goat anti-mouse, 115-035-044; Jackson ImmunoResearch, Ely, UK). Aminoethyl carbazole was used as a chromogen. A minimum of 10 pulmonary arteries with an external diameter of 30–100 µm per lung slide were examined, measuring both internal and external diameter of the media to calculate the vascular medial thickness²⁷. An observer blinded to group assignment (D.B.) performed all pulmonary histological evaluations.

Statistical analysis

Data were analyzed using Prism 9 for MacOS (GraphPad Prism, San Diego, CA, USA). Data distribution was checked for normality using a Shapiro-Wilk normality test and presented as mean with standard deviation or median with interquartile range, as appropriate. Data comparison was done by Fisher's exact, unpaired t-test or Mann Whitney U-test, depending on data characteristics. A p value of < .05 was considered significant. Adjustment for multiple testing was applied for DTI data using the Benjamini, Krieger and Yekutieli method with 10% FDR.

Declarations

Data Availability

The datasets analysed during the current study available from the corresponding author on reasonable request.

Acknowledgments

This project has received funding from the European Union's Horizon 2020 research and innovation programme under the Marie Skłodowska-Curie grant agreement No 765274.

We would like to thank the technical assistance from the G-Pure laboratory at KU Leuven, namely Katrien Luyten and Sofie Jannes, and the valuable advice from Dr. Miriam Illa from the University of Barcelona. We would also like to thank Dr. Colin Murdoch and Mirren Augustin from Dundee University and iPLACENTA for their continued support.

Author contributions

All individuals listed as authors have significantly contributed to this study. I.V. performed all the surgical procedures, placental histology assessment, and brain assessment. D.B., L.vdV. and S.V. assisted all the surgical procedures. D.B., Y.R., and A.G., performed the pulmonary functional tests and lung histological analysis. E.M. analyzed the MRI data, and B.L. processed and analyzed the CT data. J.vdM. and J.D. guided the experiments and corrected the work.

Additional Information

- Supplementary information accompanies this paper
- Competing Interests: The authors declare no competing interests

References

1. Resnik, R. Intrauterine growth restriction. *Obstetrics and gynecology*. **99**, 490–496, doi:[https://doi.org/10.1016/s0029-7844\(01\)01780-x](https://doi.org/10.1016/s0029-7844(01)01780-x). (2002).
2. Flenady, V. *et al.* Major risk factors for stillbirth in high-income countries: a systematic review and meta-analysis. *The Lancet*. **377**, 1331–1340, doi:[https://doi.org/10.1016/s0140-6736\(10\)62233-7](https://doi.org/10.1016/s0140-6736(10)62233-7) (2011).
3. Lawn, J. E. *et al.* Stillbirths: rates, risk factors, and acceleration towards 2030. *The Lancet*. **387**, 587–603, doi:[https://doi.org/10.1016/s0140-6736\(15\)00837-5](https://doi.org/10.1016/s0140-6736(15)00837-5) (2016).
4. Allanson, E. R. *et al.* The WHO application of ICD-10 to deaths during the perinatal period (ICD-PM): results from pilot database testing in South Africa and United Kingdom. *BJOG*. **123**, 2019–2028, doi:10.1111/1471-0528.14244 (2016).

5. von Beckerath, A. K. *et al.* Perinatal complications and long-term neurodevelopmental outcome of infants with intrauterine growth restriction. *American journal of obstetrics and gynecology*. **208**, 130.e131-136, doi:<https://doi.org/10.1016/j.ajog.2012.11.014> (2013).
6. Barker, D. J. Adult consequences of fetal growth restriction. *Clinical obstetrics and gynecology*. **49**, 270–283, doi:<https://doi.org/10.1097/00003081-200606000-00009> (2006).
7. Pike, K., Jane Pillow, J. & Lucas, J. S. Long term respiratory consequences of intrauterine growth restriction. *Seminars in fetal & neonatal medicine*. **17**, 92–98, doi:<https://doi.org/10.1016/j.siny.2012.01.003> (2012).
8. Pels, A. *et al.* Maternal Sildenafil vs Placebo in Pregnant Women With Severe Early-Onset Fetal Growth Restriction: A Randomized Clinical Trial. *JAMA Netw Open*. **3**, e205323, doi:<https://doi.org/10.1001/jamanetworkopen.2020.5323> (2020).
9. Satterfield, M. C. B., F. W.: Spencer, T. E.: Wu, G. Sildenafil citrate treatment enhances amino acid availability in the conceptus and fetal growth in an ovine model of intrauterine growth restriction. *The Journal of nutrition*. **140**, 251–258, doi:<https://doi.org/10.3945/jn.109.114678> (2010).
10. Dilworth, M. R. A., I.: Renshall, L. J.: Cowley, E.: Baker, P.: Greenwood, S.: Sibley, C. P.: Wareing, M. Sildenafil citrate increases fetal weight in a mouse model of fetal growth restriction with a normal vascular phenotype. *PloS one*. **8**, e77748, doi:<https://doi.org/10.1371/journal.pone.0077748> (2013).
11. Swanson, A. M. & David, A. L. Animal models of fetal growth restriction: Considerations for translational medicine. *Placenta*. **36**, 623–630, doi:<https://doi.org/10.1016/j.placenta.2015.03.003> (2015).
12. Bassan, H. *et al.* Experimental intrauterine growth retardation alters renal development. *Pediatric nephrology (Berlin, Germany)* **15**, 192–195 (2000).
13. Bleeser, T. *et al.* Effects of Maternal Abdominal Surgery on Fetal Brain Development in the Rabbit Model. *Fetal diagnosis and therapy*. **48**, 189–200, doi:<https://doi.org/10.1159/000512489> (2021).
14. Derrick, M., Drobyshevsky, A., Ji, X. & Tan, S. A model of cerebral palsy from fetal hypoxia-ischemia. *Stroke*. **38**, 731–735, doi:10.1161/01.STR.0000251445.94697.64 (2007).
15. Eastwood, M. P. *et al.* A growing animal model for neonatal repair of large diaphragmatic defects to evaluate patch function and outcome. *PloS one*. **12**, e0174332, doi:10.1371/journal.pone.0174332 (2017).
16. Eixarch, E. *et al.* An experimental model of fetal growth restriction based on selective ligation of uteroplacental vessels in the pregnant rabbit. *Fetal diagnosis and therapy*. **26**, 203–211, doi:10.1159/000264063 (2009).
17. Fischer, B., Chavatte-Palmer, P., Viebahn, C., Navarrete Santos, A. & Duranthon, V. Rabbit as a reproductive model for human health. *Reproduction (Cambridge, England)*. **144**, 1–10, doi:10.1530/REP-12-0091 (2012).
18. van der Merwe, J. *et al.* Early neuropathological and neurobehavioral consequences of preterm birth in a rabbit model. *Scientific reports*. **9**, 3506, doi:<https://doi.org/10.1038/s41598-019-39922-8> (2019).

19. Furukawa, S., Kuroda, Y. & Sugiyama, A. A comparison of the histological structure of the placenta in experimental animals. *J Toxicol Pathol.* **27**, 11–18, doi:<https://doi.org/10.1293/tox.2013-0060> (2014).
20. Lopez-Tello, J., Arias-Alvarez, M., Gonzalez-Bulnes, A. & Sferuzzi-Perri, A. N. Models of Intrauterine growth restriction and fetal programming in rabbits. *Molecular reproduction and development.* **86**, 1781–1809, doi:[10.1002/mrd.23271](https://doi.org/10.1002/mrd.23271) (2019).
21. Clancy, B., Finlay, B. L., Darlington, R. B. & Anand, K. J. Extrapolating brain development from experimental species to humans. *Neurotoxicology.* **28**, 931–937, doi:[10.1016/j.neuro.2007.01.014](https://doi.org/10.1016/j.neuro.2007.01.014) (2007).
22. Hunter, D. S. *et al.* Programming the brain: Common outcomes and gaps in knowledge from animal studies of IUGR. *Physiology & behavior.* **164**, 233–248, doi:<https://doi.org/10.1016/j.physbeh.2016.06.005> (2016).
23. Pringle, K. C. Human fetal lung development and related animal models. *Clinical obstetrics and gynecology.* **29**, 502–513 (1986).
24. Salaets, T., Gie, A., Tack, B., Deprest, J. & Toelen, J. Modelling Bronchopulmonary Dysplasia in Animals: Arguments for the Preterm Rabbit Model. *Curr Pharm Des.* **23**, 5887–5901, doi:<https://doi.org/10.2174/1381612823666170926123550> (2017).
25. Toelen, J. *et al.* The fetal respiratory system as target for antenatal therapy. *Facts, views & vision in ObGyn.* **3**, 22–35 (2011).
26. Arigliani, M., Spinelli, A. M., Liguoro, I. & Cogo, P. Nutrition and Lung Growth. *Nutrients.* **10**, doi:[10.3390/nu10070919](https://doi.org/10.3390/nu10070919) (2018).
27. Gie, A. G. *et al.* Intermittent CPAP limits hyperoxia-induced lung damage in a rabbit model of bronchopulmonary dysplasia. *American journal of physiology. Lung cellular and molecular physiology.* **318**, L976-L987, doi:<https://doi.org/10.1152/ajplung.00465.2019> (2020).
28. Jimenez, J. *et al.* Progressive Vascular Functional and Structural Damage in a Bronchopulmonary Dysplasia Model in Preterm Rabbits Exposed to Hyperoxia. *International journal of molecular sciences.* **17**, doi:<https://doi.org/10.3390/ijms17101776> (2016).
29. Salaets, T. *et al.* Preterm birth impairs postnatal lung development in the neonatal rabbit model. *Respir Res.* **21**, 59, doi:<https://doi.org/10.1186/s12931-020-1321-6> (2020).
30. van der Merwe, J. *et al.* Neurocognitive sequelae of antenatal corticosteroids in a late preterm rabbit model. *American journal of obstetrics and gynecology.* doi:[10.1016/j.ajog.2021.11.1370](https://doi.org/10.1016/j.ajog.2021.11.1370) (2021).
31. van der Merwe, J. *et al.* Earlier preterm birth is associated with a worse neurocognitive outcome in a rabbit model. *PloS one.* **16**, e0246008, doi:<https://doi.org/10.1371/journal.pone.0246008> (2021).
32. Russo, F. M. *et al.* Transplacental sildenafil rescues lung abnormalities in the rabbit model of diaphragmatic hernia. *Thorax.* **71**, 517–525, doi:<https://doi.org/10.1136/thoraxjnl-2015-207949> (2016).
33. Roubliova, X. I. *et al.* Morphologic changes and methodological issues in the rabbit experimental model for diaphragmatic hernia. *Histology and histopathology.* **25**, 1105–1116,

doi:<https://doi.org/10.14670/hh-25.1105> (2010).

34. Lopez-Tello, J. A.-A., M.: Jimenez-Martinez, M. A.: Barbero-Fernandez, A.: Garcia-Garcia, R. M.: Rodriguez, M.: Lorenzo, P. L.: Torres-Rovira, L.: Astiz, S.: Gonzalez-Bulnes, A.: Rebollar, P. G. The effects of sildenafil citrate on feto-placental development and haemodynamics in a rabbit model of intrauterine growth restriction. *Reproduction, fertility, and development*. **29**, 1239–1248, doi:<https://doi.org/10.1071/rd15330> (2017).
35. Zhang, A. Z., L. F.: Xiang, X. L.: Wang, K.: Zhou, Q.: Duan, T. Folic acid attenuates dexamethasone-induced placental growth restriction. *European review for medical and pharmacological sciences*. **19**, 1130–1140 (2015).
36. Hewitt, D. P., Mark, P. J. & Waddell, B. J. Glucocorticoids prevent the normal increase in placental vascular endothelial growth factor expression and placental vascularity during late pregnancy in the rat. *Endocrinology*. **147**, 5568–5574, doi:[10.1210/en.2006-0825](https://doi.org/10.1210/en.2006-0825) (2006).
37. Wyrwoll, C. S., Seckl, J. R. & Holmes, M. C. Altered placental function of 11beta-hydroxysteroid dehydrogenase 2 knockout mice. *Endocrinology*. **150**, 1287–1293, doi:[10.1210/en.2008-1100](https://doi.org/10.1210/en.2008-1100) (2009).
38. Guo, M. Y. W., H.: Chen, Y. H.: Xia, M. Z.: Zhang, C.: Xu, D. X. N-acetylcysteine alleviates cadmium-induced placental endoplasmic reticulum stress and fetal growth restriction in mice. *PloS one*. **13**, e0191667, doi:<https://doi.org/10.1371/journal.pone.0191667> (2018).
39. Ohta, H. K., M.: Li, H.: Sakai, H.: Okamura, K.: Yaegashi, N. Potential New Non-Invasive Therapy Using Artificial Oxygen Carriers for Pre-Eclampsia. *Journal of functional biomaterials*. **8**, doi:<https://doi.org/10.3390/jfb8030032> (2017).
40. Chen, Y. H. Z., M.: Chen, X.: Zhang, Y.: Wang, H.: Huang, Y. Y.: Wang, Z.: Zhang, Z. H.: Zhang, C.: Xu, D. X. Zinc supplementation during pregnancy protects against lipopolysaccharide-induced fetal growth restriction and demise through its anti-inflammatory effect. *Journal of immunology*. **189**, 454–463, doi:<https://doi.org/10.4049/jimmunol.1103579> (2012).
41. Jones, H. N., Crombleholme, T. & Habli, M. Adenoviral-mediated placental gene transfer of IGF-1 corrects placental insufficiency via enhanced placental glucose transport mechanisms. *PloS one*. **8**, e74632, doi:[10.1371/journal.pone.0074632](https://doi.org/10.1371/journal.pone.0074632) (2013).
42. Diaz, V., Lebras-Isabet, M. N. & Denjean, A. Effect of Nomega-nitro-L-arginine methyl ester-induced intrauterine growth restriction on postnatal lung growth in rats. *Pediatric research*. **58**, 557–561, doi:[10.1203/01.PDR.0000179398.62365.43](https://doi.org/10.1203/01.PDR.0000179398.62365.43) (2005).
43. Velten, M. B., R. D., Jr.: Heyob, K. M.: Tipple, T. E.: Rogers, L. K. Maternal dietary docosahexaenoic acid supplementation attenuates fetal growth restriction and enhances pulmonary function in a newborn mouse model of perinatal inflammation. *The Journal of nutrition*. **144**, 258–266, doi:<https://doi.org/10.3945/jn.113.179259> (2014).
44. Karnak, I., Muftuoglu, S., Cakar, N. & Tanyel, F. C. Organ growth and lung maturation in rabbit fetuses. *Res Exp Med (Berl)*. **198**, 277–287, doi:[10.1007/s004330050111](https://doi.org/10.1007/s004330050111) (1999).

45. Liu, X. *et al.* Maternal protein restriction alters VEGF signaling and decreases pulmonary alveolar in fetal rats. *International journal of clinical and experimental pathology*. **7**, 3101–3111 (2014).
46. Maritz, G. S. *et al.* Effects of fetal growth restriction on lung development before and after birth: a morphometric analysis. *Pediatric pulmonology*. **32**, 201–210 (2001).
47. Zana-Taieb, E. *et al.* Effect of two models of intrauterine growth restriction on alveolarization in rat lungs: morphometric and gene expression analysis. *PloS one*. **8**, e78326, doi:10.1371/journal.pone.0078326 (2013).
48. Khazaee, R., McCaig, L. A., Yamashita, C., Hardy, D. B. & Veldhuizen, R. A. W. Maternal protein restriction during perinatal life affects lung mechanics and the surfactant system during early postnatal life in female rats. *PloS one*. **14**, e0215611, doi:10.1371/journal.pone.0215611 (2019).
49. Huang, L. T., Chou, H. C., Lin, C. M. & Chen, C. M. Uteroplacental Insufficiency Alters the Retinoid Pathway and Lung Development in Newborn Rats. *Pediatr Neonatol*. **57**, 508–514, doi:10.1016/j.pedneo.2016.03.003 (2016).
50. Joss-Moore, L. *et al.* Intrauterine growth restriction transiently delays alveolar formation and disrupts retinoic acid receptor expression in the lung of female rat pups. *Pediatric research*. **73**, 612–620, doi:10.1038/pr.2013.38 (2013).
51. McGillick, E. V., Orgeig, S. & Morrison, J. L. Regulation of lung maturation by prolyl hydroxylase domain inhibition in the lung of the normally grown and placentally restricted fetus in late gestation. *American journal of physiology. Regulatory, integrative and comparative physiology*. **310**, R1226-1243, doi:10.1152/ajpregu.00469.2015 (2016).
52. Orgeig, S. *et al.* Increased lung prolyl hydroxylase and decreased glucocorticoid receptor are related to decreased surfactant protein in the growth-restricted sheep fetus. *American journal of physiology. Lung cellular and molecular physiology*. **309**, L84-97, doi:10.1152/ajplung.00275.2014 (2015).
53. Dravet-Gounot, P. *et al.* Lung microRNA deregulation associated with impaired alveolarization in rats after intrauterine growth restriction. *PloS one*. **12**, e0190445, doi:10.1371/journal.pone.0190445 (2017).
54. Eixarch, E. *et al.* Neonatal neurobehavior and diffusion MRI changes in brain reorganization due to intrauterine growth restriction in a rabbit model. *PloS one*. **7**, e31497, doi:10.1371/journal.pone.0031497 (2012).
55. Illa, M. *et al.* Early Environmental Enrichment Enhances Abnormal Brain Connectivity in a Rabbit Model of Intrauterine Growth Restriction. *Fetal diagnosis and therapy*. **44**, 184–193, doi:10.1159/000481171 (2018).
56. Saito, A. *et al.* Behavioral abnormalities of fetal growth retardation model rats with reduced amounts of brain proteoglycans. *Exp Neurol*. **219**, 81–92, doi:10.1016/j.expneurol.2009.04.012 (2009).
57. Villescas, R., Van Marthens, E. & Hammer, R. P., Jr. Prenatal undernutrition: effects on behavior, brain chemistry and neuroanatomy in rats. *Pharmacol Biochem Behav*. **14**, 455–462, doi:10.1016/0091-3057(81)90302-6 (1981).

58. Zhang, Y., Li, N., Yang, J., Zhang, T. & Yang, Z. Effects of maternal food restriction on physical growth and neurobehavior in newborn Wistar rats. *Brain Res Bull.* **83**, 1–8, doi:10.1016/j.brainresbull.2010.06.005 (2010).
59. Hernandez-Andrade, E., Figueroa-Diesel, H., Jansson, T., Rangel-Nava, H. & Gratacos, E. Changes in regional fetal cerebral blood flow perfusion in relation to hemodynamic deterioration in severely growth-restricted fetuses. *Ultrasound in obstetrics & gynecology.* **32**, 71–76, doi:10.1002/uog.5377 (2008).
60. Kalusa, M., Heinrich, M. D., Sauerland, C., Morawski, M. & Fietz, S. A. Developmental Differences in Neocortex Neurogenesis and Maturation Between the Altricial Dwarf Rabbit and Precocial Guinea Pig. *Front Neuroanat.* **15**, 678385, doi:10.3389/fnana.2021.678385 (2021).
61. Herrera, E. A. *et al.* Assessment of in vivo fetal growth and placental vascular function in a novel intrauterine growth restriction model of progressive uterine artery occlusion in guinea pigs. *The Journal of physiology.* **594**, 1553–1561, doi:10.1113/JP271467 (2016).
62. Tsuji, M., Coq, J. O., Ogawa, Y., Yamamoto, Y. & Ohshima, M. A Rat Model of Mild Intrauterine Hypoperfusion with Microcoil Stenosis. *J Vis Exp.* doi:10.3791/56723 (2018).
63. Percie du Sert, N. *et al.* The ARRIVE guidelines 2.0: Updated guidelines for reporting animal research. *PLoS biology.* **18**, e3000410, doi:10.1371/journal.pbio.3000410 (2020).
64. Bankhead, P. *et al.* QuPath: Open source software for digital pathology image analysis. *Scientific reports.* **7**, 16878, doi:10.1038/s41598-017-17204-5 (2017).
65. De Clercq, K., Lopez-Tello, J., Vriens, J. & Sferruzzi-Perri, A. N. Double-label immunohistochemistry to assess labyrinth structure of the mouse placenta with stereology. *Placenta.* **94**, 44–47, doi:10.1016/j.placenta.2020.03.014 (2020).
66. Derrick, M. *et al.* Preterm fetal hypoxia-ischemia causes hypertonia and motor deficits in the neonatal rabbit: a model for human cerebral palsy? *J Neurosci.* **24**, 24–34, doi:10.1523/JNEUROSCI.2816-03.2004 (2004).
67. Ferraris, S. *et al.* A magnetic resonance multi-atlas for the neonatal rabbit brain. *Neuroimage.* **179**, 187–198, doi:10.1016/j.neuroimage.2018.06.029 (2018).
68. Fick, R. H. J., Wassermann, D. & Deriche, R. The Dmipy Toolbox: Diffusion MRI Multi-Compartment Modeling and Microstructure Recovery Made Easy. *Front Neuroinform.* **13**, 64, doi:10.3389/fninf.2019.00064 (2019).
69. Garyfallidis, E. *et al.* Dipy, a library for the analysis of diffusion MRI data. *Front Neuroinform.* **8**, 8, doi:10.3389/fninf.2014.00008 (2014).
70. Richter, J. *et al.* Functional assessment of hyperoxia-induced lung injury after preterm birth in the rabbit. *American journal of physiology. Lung cellular and molecular physiology.* **306**, L277-283, doi:https://doi.org/10.1152/ajplung.00315.2013 (2014).
71. Salaets, T. *et al.* A semi-automated method for unbiased alveolar morphometry: Validation in a bronchopulmonary dysplasia model. *PloS one.* **15**, e0239562, doi:https://doi.org/10.1371/journal.pone.0239562 (2020).

Figures

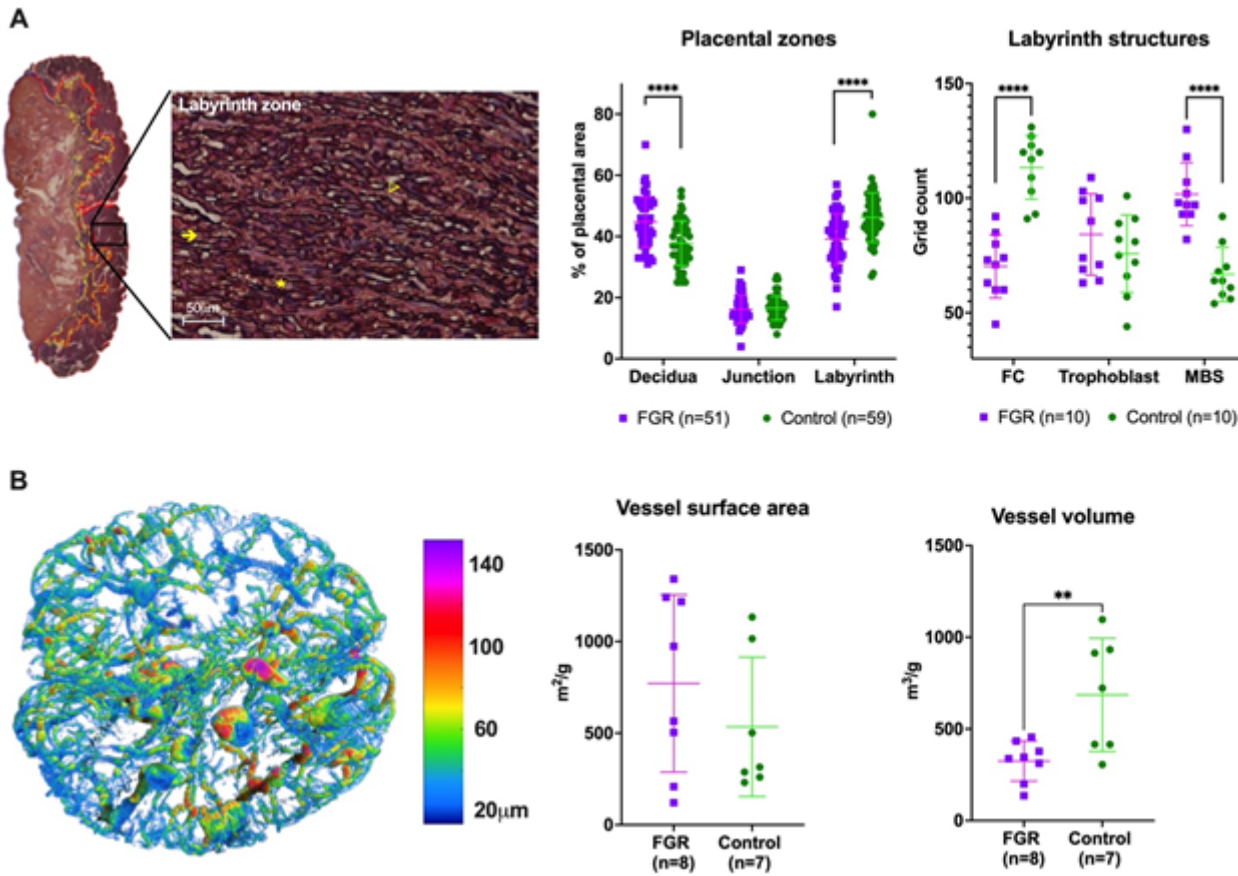


Figure 1

Placental histology and microcomputed tomography. A. Placenta with cytokeratin/lectin double staining, divided by placental zones (left image). Within the labyrinth (zoomed), fetal capillaries (star), maternal blood spaces (arrow) and trophoblast (arrowhead) were grid counted and expressed as relative areas. B. Representative image of placental microcomputed tomography after color coding according to vessel diameter. Data displayed as mean \pm SD with significance as $*0.05 \geq p > 0.01$; $** 0.01 \geq p > 0.001$.; $***0.001 > p > 0.0001$; $**** p < 0.0001$.

displayed as median and IQR (A) or mean and SD (B, C) with significance as $*0.05 \geq p > 0.01$; $** 0.01 \geq p > 0.001$.; $***0.001 > p > 0.0001$; $**** p < 0.0001$.

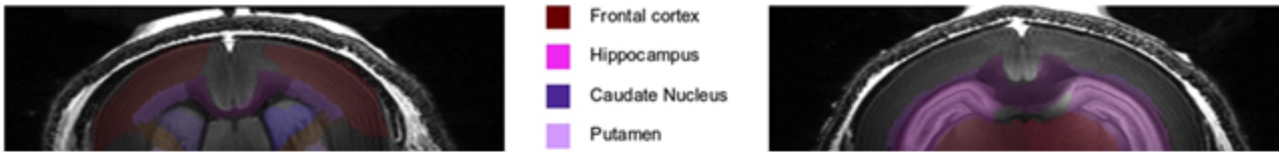


Figure 3

Ex vivo brain diffusion tensor metrics at postnatal day 1. Data displayed as median and IQR with significance as $*0.05 \geq p > 0.01$; $** 0.01 \geq p > 0.001$. Correction for multiple comparison by Benjamini, Krieger and Yekutieli method with 10% FDR.

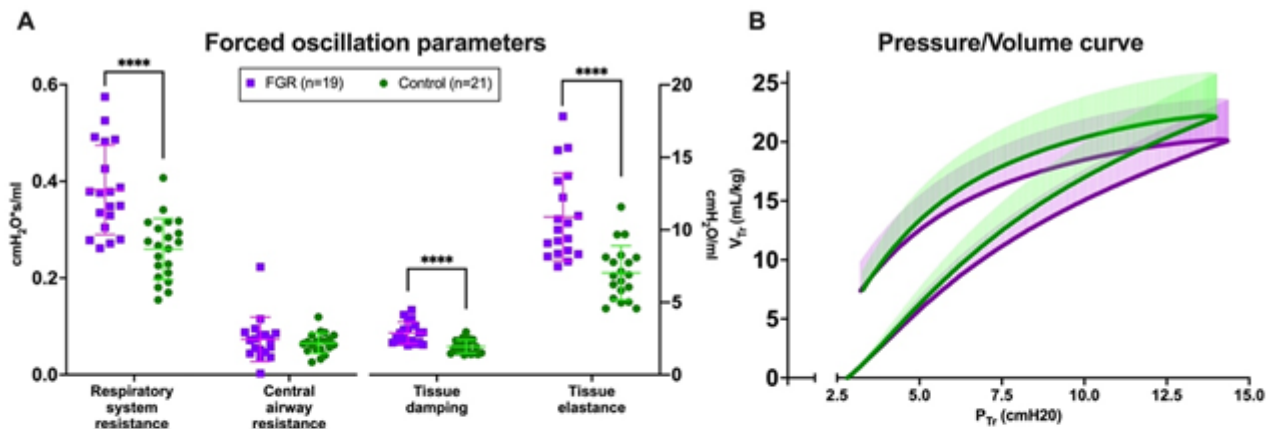


Figure 4

Pulmonary functional tests at postnatal day 1. A. Forced oscillation test results. B. Pressure/volume loop. C. Representative images of histological H&E-stained slides and alveolar architecture data. Data displayed as mean \pm SD, with significance as * $0.05 \geq p > 0.01$; ** $0.01 \geq p > 0.001$; *** $0.001 > p > 0.0001$; **** $p < 0.0001$.

Supplementary Files

This is a list of supplementary files associated with this preprint. Click to download.

- [Supplementaryinformation.docx](#)